International Journal for Multidisciplinary Research (IJFMR)
E-ISSN: 2582-2160 ● Website: www.ijfmr.com ● Email: editor@ijfmr.com

Non-Darcy Convective Heat Transport in an Al_2O_3–Cu–SiO_2–TiO_2/Ethylene-Glycol Tetra-Hybrid Coolant over a Stretched Sheet: Coupled Role of Thermal Dispersion, Arrhenius Exothermicity and Dual Interfacial Slip

H. G. Suguna[1], P. Chandrakala[2]

[1]Associate Professor, Department of Mathematics, GFGC, Sidlaghatta, Chikkaballapur (Dt), Karnataka, India.

[2]Department of Mathematics, School of Engineering, Anurag University, Hyderabad-500 088, Telangana, India.

Abstract

The thermal budget of compact, high-flux hardware is set by the coolant long before it is set by the geometry, and multi-component nanoparticle suspensions are among the most promising means of relaxing that constraint. This paper reports a numerical study of steady, laminar, two-dimensional magnetohydrodynamic heat transport in a four-component suspension — Al_2O_3, Cu, SiO_2 and TiO_2 dispersed in ethylene glycol — driven by a linearly stretched sheet embedded in a Darcy–Forchheimer porous matrix. A single energy balance is assembled in which hydrodynamic thermal dispersion, an exothermic step of modified-Arrhenius type, nonlinear radiative flux, thermally sensitive viscosity, conductivity and electrical conductivity, Joule heating and frictional dissipation all act together, while velocity and thermal slips are imposed at the wall. Similarity variables collapse the partial differential system to a coupled pair of ordinary differential equations, which is integrated by the embedded Runge–Kutta–Fehlberg (RKF-45) pair driven by a shooting iteration. Iteration histories and mesh-refinement trials establish the reliability of the solver, and reduction of the model to previously documented limits reproduce published wall temperature gradients to better than 0.11%. The computations show that thermal dispersion redistributes energy within the layer and sharpens the wall gradient, that radiative flux together with the exothermic step lifts the temperature field, and that magnetic and porous drag retard the stream while raising its temperature. Compared under identical settings with three- and two-particle counterparts, the four-particle suspension sustains the largest velocity and temperature profiles and a wall shear stress 37–39% above that of the two-particle fluid, together with the highest wall heat-transfer rate throughout the parameter space examined.

Keywords: Tetra-hybrid nanofluid; thermal dispersion; Arrhenius exothermicity; velocity and thermal slip; non-Darcy porous matrix; nonlinear thermal radiation.

1. Introduction

Thermal management has become the limiting design constraint across a widening range of engineering hardware. Processor packages, power-electronic modules, concentrating solar receivers and compact exchangers all now dissipate heat fluxes that the conventional carrier liquids — water, oils, ethylene glycol cannot remove at acceptable pumping cost, simply because the thermal conductivity of a molecular liquid is one to three orders of magnitude below that of the solids surrounding it. Dispersing solid particles of nanometre dimension in such a carrier is the direct response to that mismatch: the resulting colloid inherits part of the conductivity of the solid phase while retaining the handling characteristics of a liquid. Chamkha et al. [1] documented the gains available from this route in enclosure convection, and Jan et al. [2] extended the analysis to curved stretching geometries under an imposed magnetic field. Once the idea of loading a carrier with one species is accepted, there is no reason to stop at one. Conventional coolants often reach critical thermal limitations in compact high-flux systems, where traditional single-phase fluids fail to provide adequate heat removal efficiency due to restricted convective capacity [3]. To address these bottlenecks, the integration of multicomponent nanofluids—specifically those containing Al2O3, Cu, SiO2, and TiO2—offers a synergistic approach to significantly augment thermal conductivity and optimize heat dissipation [4]. The dispersion of these distinct nanoparticle species into an ethylene glycol base exploits their collective thermophysical properties to mitigate the resistance posed by Darcy–Forchheimer porous structures [5]. Such tetra-hybrid formulations provide enhanced control over heat transfer rates, allowing for the precise tailoring of thermofluidic performance to meet the rigorous demands of modern industrial applications [6].

A second and quite separate route to augmented heat transport becomes available when the flow is confined within a permeable solid skeleton. Fluid filaments threading a granular matrix are repeatedly split, deflected and rejoined by the grains they encounter, and the resulting pore-scale stirring transports energy in addition to — and independently of — molecular conduction. Kvernvold and Tyvand [7] supplied dispersive heat-transport measurements in close agreement with theoretical prediction, Cheng [8] established the non-Darcian formulation on which most later work rests, and Telles and Trevisan [9] gave the velocity-proportional closure for the dispersive conductivity that is adopted in the present model.

Furthermore, the incorporation of thermal dispersion and exothermic chemical reactions within this complex fluid architecture compensates for the reduced velocity profiles inherent in porous media flow [10, 11]. The synergistic interaction of these nanoparticles not only compensates for convective thermal constraints but also broadens the operational efficacy of the base fluid under extreme conditions [12, 13]. By integrating magnetohydrodynamic forces and Joule heating, this analytical framework also addresses the critical thermal management requirements of high-performance energy systems where conventional fluids lack sufficient cooling capacity [14]. Moreover, the implementation of slip boundary conditions and radiative flux mechanisms serves to regulate the temperature-dependent viscous behavior, ensuring that energy conversion processes remain stable amidst high-intensity exothermic outputs [15, 16]. This investigation thus seeks to evaluate the underlying fluid dynamics and entropy generation mechanisms that define this multicomponent system's performance in high-flux environments [17, 18], providing a nuanced understanding of how ternary and quaternary additives surpass traditional binary hybrid fluids in mitigating entropy generation [19].

The final ingredient concerns what happens at the wall itself. The no-slip and no-jump conditions of classical boundary-layer theory presume perfect mechanical and thermal contact between liquid and solid, and that presumption fails for structured liquids — particulate suspensions, emulsions, foams — and at

small scales generally. A finite tangential velocity at the surface lowers the shear drag and raises throughput, while a temperature jump expresses a finite interfacial thermal resistance and cannot be omitted if the thermal field is to be predicted reliably. Khan and Rasheed [20] quantified both effects for a hybrid nanofluid over an irregular three-dimensional surface, Mingyu and Jing [21] examined velocity and temperature slips in thermal elastohydrodynamic contact, Maranna et al. [22] treated Navier slip in magnetohydrodynamic hybrid-nanofluid flow over a porous stretching sheet,

Reviewing this literature, three gaps are apparent. First, thermal dispersion and multi-component suspensions have been developed largely in isolation, so the question of whether the two augmentation mechanisms reinforce each other remains open. Second, exothermic Arrhenius heat release has been studied mainly for single-component or binary fluids and rarely alongside nonlinear radiation, Joule heating and variable properties within one energy balance. Third, the comparisons between tetra-, ternary- and binary-hybrid fluids that appear in the literature are usually drawn from different studies using different closures, so the reported superiority of the four-particle fluid is difficult to attribute to composition alone. The present work addresses all three by solving a single, fully coupled formulation in which thermal dispersion, a modified-Arrhenius exothermic source, nonlinear radiation, Lorentz drag, Joule and viscous heating, thermally sensitive properties and dual interfacial slip act simultaneously, and by evaluating the two-, three- and four-particle suspensions throughout on one identical set of thermophysical inputs.

1.1. Distinctive features of the present work

- a strictly controlled comparison of the four-particle suspension (Al_2O_3 + Cu + SiO_2 + TiO_2/EG) with its three-particle (Al_2O_3 + Cu + SiO_2/EG) and two-particle (Al_2O_3 + Cu/EG) analogues, evaluated throughout on one identical set of thermophysical inputs;
- the simultaneous retention, within a single energy balance, of velocity-proportional thermal dispersion, nonlinear radiative exchange, Ohmic and frictional heating and a modified-Arrhenius exothermic source — a grouping seldom carried together;
- the imposition of independent velocity and thermal slips on an advanced multi-component suspension flowing over a stretched sheet embedded in a Darcy–Forchheimer matrix;
- an assessment of the extent to which dispersive and molecular conduction reinforce one another as the number of dispersed species is increased; and
- a unified appraisal of thermal effectiveness across the two-, three- and four-particle fluids, from which design guidance for next-generation thermal hardware is drawn.

1.2. Engineering context and fields of application

Configurations of the kind analysed here underpin a broad range of energy-related and biomedical technologies, among them:

- solar-thermal absorbers and ambient-energy harvesting devices, whose conversion efficiency improves as the effective conductivity of the working liquid rises;
- high-flux cooling of processors, electronic assemblies and data-centre hardware;
- reactors and catalytic vessels in which strongly exothermic chemistry releases substantial heat;
- metal-processing and polymer-extrusion lines, where the stretching of a sheet is an everyday operation;
- coolant loops in nuclear plant, where efficient heat removal must be combined with thermal stability;
- nanoparticle-based hyperthermia and other thermally mediated biomedical procedures;
- thermal control of engines and components in road-vehicle and aerospace structures; and

- exchangers, refrigeration equipment and thermal-storage plant, whose operating efficiency benefits directly from the enhanced transport that tetra-hybrid liquids offer.

2. Mathematical formulation

The configuration treated here is a steady, laminar, incompressible and two-dimensional stream of a tetra-hybrid nanofluid driven by a linearly stretched sheet. Ethylene glycol acts as the carrier and receives four distinct solids — Al_2O_3, Cu, SiO_2 and TiO_2 — which together constitute the composite liquid; Fig. 1 shows the geometry. The model rests on the following premises:

- the suspension is treated as a homogeneous single-phase medium of effective properties, so that the thermal field is the only transported scalar and no species balance is required;
- velocity-proportional thermal dispersion, nonlinear radiative transfer, Joule heating, viscous dissipation, internal generation and an exothermic Arrhenius source are all retained in the energy equation;
- the reactant sustaining the exothermic step is present in large excess, so its depletion over the residence time of the layer is negligible and the reaction enters as a temperature-dependent volumetric heat source;
- the inertial correction of Darcy's law in the Forchheimer sense is included, and the fluid occupies the half-space $y \geq 0$;
- the motion originates in linear stretching of the wall about the slit at $x = y = 0$, the surface speed being $u_w(x) = ax$ with $a > 0$ constant;
- the wall temperature is T_w, decaying to the free-stream level T_∞ remote from the sheet; and
- slips in velocity and in temperature are imposed at the boundary.

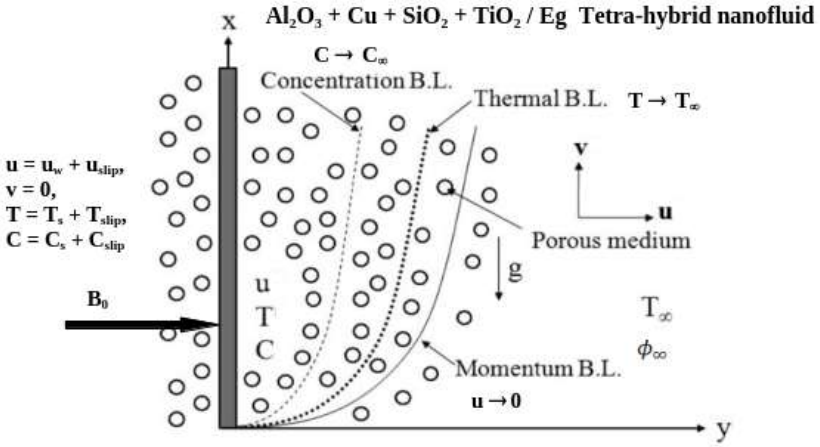


Fig. 1. Flow geometry and coordinate frame.

On these premises the balances of mass, momentum and energy are written as [23, 24]:

$$\frac{\partial u}{\partial x}+\frac{\partial v}{\partial y}=0 \tag{1}$$

$$\rho_{tehnf}\left(u\frac{\partial u}{\partial x}+v\frac{\partial u}{\partial y}\right)=\frac{\partial}{\partial y}\left[\mu_{tehnf}\frac{\partial u}{\partial y}\right]-\frac{\mu_{tehnf}}{k}(u)-\frac{Cb}{\sqrt{k}}(u^2)+$$

$$(\rho)_{thnf}\, g[\beta_{tehnf}(T-T_\infty)+\beta^2{}_{tehnf}(T-T_\infty)^2]+\sigma_{tehnf}(EB-B^2u) \tag{2}$$

$$(\rho C_p)_{tehnf}(u\frac{\partial T}{\partial x}+v\frac{\partial T}{\partial y})=\frac{\partial}{\partial \vec{x}}(\alpha_x\frac{\partial T}{\partial \vec{x}})+\frac{\partial}{\partial \vec{y}}((\alpha_y\frac{\partial T}{\partial \vec{y}})-\frac{\partial q_r}{\partial y}$$
$$+Q_H(T-T_\infty)+\tau[D_B(\frac{\partial T}{\partial y}\frac{\partial C}{\partial y})+\frac{D_T}{T_\infty}(\frac{\partial T}{\partial y})^2]+\mu_{tehnf}(\frac{\partial u}{\partial y})^2+\sigma_{tehnf}(T,C)\mu_e^2H_o^2(u^2)$$
$$+Q_1^{'}A(C-C_\infty)(C-C_\infty)(\frac{T}{T_\infty})^n Exp(-\frac{E_a}{KT}) \quad (3)$$

Here u and v are the velocity components resolved along x and y. The symbols $(\rho C_p)_{thnf}$, ρ_{thnf}, μ_{thnf}, k_{thnf}, β_{thnf} and σ_{thnf} refer to the four-particle suspension and denote, in order, its capacity to store heat, its mass per unit volume, its resistance to shear, its ability to conduct energy, its expansion on heating and its ability to carry current. The spatially varying inertia coefficient of the matrix appears as F, the volumetric rate of internal generation as Q_H, and the heat of reaction, rate constant and reactant loading of the exothermic step as Q_R, k_r and C_0 respectively, with E_a the activation energy and κ the Boltzmann constant. Following Telles and Trevisan [24], molecular and hydrodynamic transport of energy are combined by writing the dispersive conductivity as $k_d = (\rho C_p)_f \gamma_1 d\, u$, in which d is the mean pore diameter and γ_1 the mechanical-dispersion coefficient, so that the augmentation is proportional to the local velocity and therefore largest where the stirring is most vigorous.

In line with Seddeek and Salem [25], a linear temperature dependence is assigned to the thermal conductivity, $k = k_\infty(1+\varepsilon\theta)$, whereas the viscosity decays exponentially with temperature, $\mu=\mu_\infty e^{-m\theta}$. The electrical conductivity is likewise allowed to vary, $\sigma(T) = \sigma_{thnf}[1 + A\theta]$, and radiative transfer is represented through the Rosseland diffusion approximation,

$$q_r = -(4\sigma/3k)\,\partial T^4/\partial y \quad (4)$$

The fourth-power dependence is retained in full rather than linearised, so that the effective radiative conductivity carries the factor $(1 + \delta\theta)^3$ and the formulation remains valid at the large wall-to-ambient temperature ratios encountered in solar and reactor applications.

Conditions at the wall and in the far field, incorporating both slip mechanisms, are taken as:

$$\text{at } y = 0: \quad u = u_w(x) + N_1\mu(T)\,\partial u/\partial y, \quad v = 0, \quad T = T_w + D_1\,\partial T/\partial y \quad (5)$$
$$\text{as } y \to \infty: \quad u \to 0, \quad T \to T_\infty \quad (6)$$

in which N_1 is the Navier slip length and D_1 the thermal-jump coefficient, the latter expressing the finite interfacial resistance between the heated surface and the liquid.

With the stream function and the similarity variable defined after [26],

$$\eta=(\sqrt{\frac{a}{\nu_f}})y, u=axf'(\eta), v=-(\sqrt{(a\nu_f)})f(\eta),\ \theta=\frac{T-T_\infty}{T_w-T_\infty}, \Phi=\frac{C-C_\infty}{C_w-C_\infty} \quad (7)$$

the system collapses to the coupled nonlinear ordinary differential equations

$$f'''-Bf'\theta'-A_1Kf'+e^{B\theta}[A_1(ff''-(f')^2]-(\frac{A_1A_6}{A_2})M^2(1+\varepsilon_1\theta+\varepsilon_2\Phi)(f')$$
$$+(\frac{GA_1A_3}{A_2})(\theta+\beta_1\theta^2)-(\frac{A_1}{A_2})fs(f')^2 \quad (8)$$

$$\begin{aligned}&(1+\beta_{11}\theta+A_4+\frac{4Rd}{3})\theta''+\beta_{11}(\theta')^2+\Pr(A_3)(f\theta')+Rd(\theta_w-1)^3(3\theta^2(\theta')^2+\theta^3\theta'')\\&+3Rd(\theta_w-1)[(\theta_w-1)+1)](2\theta^2(\theta')^2+\theta^2\theta'')+Q(\theta)+e^{-B\theta}Ec\Pr[(f'')^2+(g')^2]\\&+Ec\Pr A_6M^2(1+\varepsilon_1\theta+\varepsilon_2\Phi)((f')^2+g^2)+Ds(f''\theta'+f'\theta'')=0\end{aligned} \quad (9)$$

together with the transformed wall and far-field conditions

$$f(0)=0,\quad f'(0)=1+B_1f''(0),\quad \theta(0)=1+B_2\theta'(0);\quad f'(\eta)\to 0,\ \theta(\eta)\to 0\ \text{as}\ \eta\to\infty \quad (10)$$

The property ratios $A_1=\rho_{thnf}/\rho_f$, $A_2=\sigma_{thnf}/\sigma_f$, $A_3=(\rho\beta)_{thnf}/(\rho\beta)_f$, $A_4=(\rho C_p)_{thnf}/(\rho C_p)_f$ and $A_5=k_{thnf}/k_f$ carry the entire influence of composition. Several dimensionless groups appear in Eqs. (8)–(10). Property variation is measured by ε_1 for viscosity, ε_2 for thermal conductivity and A for electrical conductivity. Resistance to the motion enters through the inverse-Darcy number K, the Forchheimer number f_s and the magnetic parameter M, buoyant forcing through the Grashof number G, and wall slippage through B_1 and B_2. Diffusive transport is characterised by the Prandtl number Pr and the thermal-dispersion parameter $D_s = \gamma_1 d\ a\ x/\nu_f$. Thermal forcing is carried by R_d for radiation, Ec for frictional heating and Q for internal generation, while the exothermic step is described by the Frank–Kamenetskii number Q_1, the activation-energy parameter $E_1=E_a/(\kappa T_\infty)$, the temperature ratio $\delta=(T_w-T_\infty)/T_\infty$ and the fitted temperature exponent n of the modified-Arrhenius rate constant.

Two quantities evaluated at the sheet are of practical interest: the drag coefficient and the dimensionless rate of heat transfer. Each follows directly from the computed wall gradients $f''(0)$ and $-\theta'(0)$, which fix respectively the shear borne by the surface and the interfacial flux of energy:

$$C_{f_x}=\frac{f''(0)}{(1-\phi)^{2.5}\,\mathrm{Re}_x^{1/2}},\quad Nu_x=-(1+Rd\theta_w)^2\theta'(0)\,\mathrm{Re}_x^{1/2} \quad (11)$$

2.1. Effective properties of the suspension

Effective values of the dynamic viscosity, the density, the thermal conductivity, the heat capacitance, the electrical conductivity and the thermal-expansion coefficient of the four-particle suspension are obtained from the mixture rules collected in Table 2, evaluated with the constituent data listed in Table 1. Throughout, φ_1, φ_2, φ_3 and φ_4 denote the volume fractions of Al_2O_3, Cu, SiO_2 and TiO_2, and $\varphi=\varphi_1+\varphi_2+\varphi_3+\varphi_4$ is the total solid loading. Setting $\varphi_4=0$ recovers the ternary hybrid and $\varphi_3=\varphi_4=0$ the binary hybrid, so that all three fluids are generated from one set of correlations and the comparison rests on composition alone.

Table 1. Thermophysical data for the four nanoparticle species and the carrier liquid.

Property	Al_2O_3	Cu	SiO_2	TiO_2	Ethylene glycol
ρ (kg m^{-3})	3970	8933	2200	4250	1115
C_p (J kg^{-1} K^{-1})	765	385	703	686.2	2430
k (W m^{-1} K^{-1})	40	401	1.2	8.8538	0.253
$\beta\times10^{-5}$ (K^{-1})	0.85	1.67	0.056	0.90	5.7
σ (S m^{-1})	1.0×10^{-10}	5.96×10^{7}	1.5×10^{-25}	6.27×10^{-5}	10.7×10^{-5}

Table 2. **Mixture correlations adopted for the effective properties of the tetra-hybrid nanofluid (i = 1…4).**

Thermophysical property	**Tetra Hybrid Nanofluid**
Density, ρ ($kg\ m^{-3}$)	$(\rho)_{tehnf} = (1-\phi_4)[(1-\phi_3[(1-\phi_1)+(1-\phi_2)\rho_f + \phi_{1\rho_{s1}}) + \phi_2\rho_{s2}] + \phi_4\rho_{s4}$
Dynamic viscosity, μ (μ) ($N\ s\ m^{-2}$)	$\mu_{tehnf} = \frac{\mu_f}{(1-\phi_1)^{2.5}(1-\phi_2)^{2.5}(1-\phi_3)^{2.5}(1-\phi_4)^{2.5}}$
Specific heat capacity, Cp ($J\ kg^{-1}\ K^{-1}$)	$(\rho C_p)_{tehnf} = (1-\phi_4)[(1-\phi_3)[(1-\phi_1)+(1-\phi_2)$ $(\rho C_p)_f + \phi_1(\rho C_p)_{s1}] + \phi_2\rho_{s2}] + \phi_4(\rho C_p)_{s4}$
Thermal conductivity, k ($W\ m^{-1}\ K^{-1}$)	$\frac{k_{nf}}{k_f} = \frac{k_{s1}+2k_f-2\phi_1(k_f-k_{s1})}{k_{s1}+2k_f+\phi_1(k_f-k_{s1})}$ $\frac{k_{hnf}}{k_{nf}} = \frac{k_{s2}+2k_{nf}-2\phi_2(k_{nf}-k_{s2})}{k_{s2}+2k_{nf}+\phi_2(k_{nf}-k_{s2})}$ $\frac{k_{thnf}}{k_{hnf}} = \frac{k_{s3}+2k_{hnf}-2\phi_3(k_{hnf}-k_{s3})}{k_{s3}+2k_{hnf}+\phi_3(k_{hnf}-k_{s3})}$ $\frac{k_{tehnf}}{k_{thnf}} = \frac{k_{s4}+2k_{thnf}-2\phi_4(k_{thnf}-k_{s4})}{k_{s4}+2k_{thnf}+\phi_4(k_{thnf}-k_{s4})}$
Thermal-expansion coefficient, β × 10−5 (K^{-1})	$(\rho\beta_p)_{tehnf} = (1-\phi_4)[(1-\phi_3)[(1-\phi_1)+(1-\phi_2)$ $(\rho\beta)_f + \phi_1(\rho\beta)_{s1}] + \phi_2\rho_{s2}] + \phi_4(\rho\beta)_{s4}$
Electrical conductivity, σ ($S\ m^{-1}$)	$\frac{\sigma_{nf}}{\sigma_f} = \frac{\sigma_{s1}+2\sigma_f-2\phi_1(\sigma_f-\sigma_{s1})}{\sigma_{s1}+2\sigma_f+\phi_1(\sigma_f-\sigma_{s1}}$ $\frac{\sigma_{hnf}}{\sigma_{nf}} = \frac{\sigma_{s2}+2\sigma_{nf}-2\phi_2(\sigma_f-\sigma_{s2})}{\sigma_{s2}+2\sigma_f+\phi_2(\sigma_f-\sigma_{s2})}$ $\frac{\sigma_{thnf}}{\sigma_{hnf}} = \frac{\sigma_{s3}+2\sigma_{hnf}-2\phi_3(\sigma_f-\sigma_{s3})}{\sigma_{s3}+2\sigma_f+\phi_3(\sigma_f-\sigma}$ $\frac{\sigma_{tehnf}}{\sigma_{thnf}} = \frac{\sigma_{s4}+2\sigma_{thnf}-2\phi_4(\sigma_f-\sigma_{s4})}{\sigma_{s4}+2\sigma_f+\phi_4(\sigma_f-\sigma_{s4}}$

3. Solution procedure

Equations (8) and (9), taken with the slip conditions (10), constitute a strongly nonlinear and fully coupled set for which no analytical solution is available. Integration is therefore performed numerically using the embedded fourth- and fifth-order Runge–Kutta–Fehlberg pair (RKF-45) driven by a shooting iteration.

3.1. Reduction to an initial-value problem

Reduction is achieved by introducing the state variables $y_1 = f$, $y_2 = f'$, $y_3 = f''$, $y_4 = \theta$ and $y_5 = \theta'$, which

recast the third- and second-order equations as a system of five first-order equations. The two wall gradients $f''(0)$ and $\theta'(0)$ that are not prescribed are assigned trial values, integration proceeds from $\eta = 0$ out to the truncated edge η_∞, and the trials are corrected by a secant update until the outer conditions are satisfied to the required tolerance.

3.2. The RKF-45 integrator

Six weighted slope evaluations are performed at every step, from which fourth- and fifth-order estimates of the solution are assembled. Their difference serves as a local error measure and drives the adaptive step-length logic: the step contracts whenever the estimated error exceeds the prescribed bound and expands when the accuracy criterion is comfortably met. Error control embedded in this manner secures high accuracy at low computational cost and removes any need to repeat the integration on successively halved meshes.

3.3. Convergence behaviour

Two independent criteria are enforced. The step size is regulated so that the local truncation error nowhere exceeds 10^{-6}, and the outer iteration is halted only once the residual $\max\{|f'(\eta_\infty)|, |\theta(\eta_\infty)|\}$ has fallen below the same bound. The iteration record obtained for the reference tetra-nanofluid case is set out in Table 3. Five passes suffice to fix the skin-friction and Nusselt functions to six significant figures, and the residual decays quadratically, so that the coupled scheme converges quickly and without oscillation.

Table 3. **Iteration record of the shooting/RKF-45 procedure for the reference tetra-nanofluid case.**

Iteration	$f''(0)$	$-\theta'(0)$	Boundary residual
1	−1.41526	1.90874	3.7×10^{-1}
2	−1.40213	1.93066	8.2×10^{-3}
3	−1.39842	1.94168	4.1×10^{-4}
4	−1.39805	1.94219	9.5×10^{-6}
5	−1.39805	1.94221	6.0×10^{-7}

4. Code verification

Confidence in the solver was established by stripping the model down to the reduced case $K = B_1 = B_2 = M = R_d = Q = Ec = Q_1 = 0$ with the solid loading removed, evaluating the wall heat-transfer function $-\theta'(0)$ across a range of Prandtl numbers, and setting the outcome beside three independent data sets [47, 48, 49]. Agreement to within 0.11% is confirmed in Table 5, the widest discrepancy occurring at $Pr = 0.72$, while from $Pr = 10$ upward at least four significant figures coincide. Table 6 reports a second check, in which the computed skin friction for the two-, three- and four-particle suspensions is placed against the results of [47]; the correspondence is again close throughout the tabulated range.

Table 4. **Values of $-\theta'(0)$ at several Prandtl numbers on a stretching sheet in the reduced case $K = B_1 = B_2 = M = R_d = Q = Ec = Q_1 = 0$ with $\varphi_i = 0$.**

Pr	Kausar et al. [48]	Grubka & Bobba [49]	Choudhary et al. [47]	Present
0.72	1.09006	1.0885	1.087788	1.088982

Pr	Kausar et al. [48]	Grubka & Bobba [49]	Choudhary et al. [47]	Present
10	1.33333	1.3333	1.333328	1.333330
30	2.50955	2.5097	2.509705	2.509701
100	4.79677	4.7969	4.796690	4.796690
1000	15.7118	15.7120	15.71153	15.71192

Table 5. **Wall shear f″(0) for the two-, three- and four-particle suspensions at $D_s = 0$, $B_1 = 0.5$ and $B_2 = 0.2$.**

M	K	Hybrid [47]	Ternary [47]	Tetra [47]	Hybrid (present)	Ternary (present)	Tetra (present)
0.1	0.2	−1.0179	−1.18424	−1.39805	−1.0180	−1.18429	−1.39801
0.2	0.2	−1.0288	−1.20009	−1.42061	−1.0287	−1.20007	−1.42064
0.3	0.2	−1.0344	−1.21018	−1.43121	−1.0349	−1.21016	−1.43126
0.1	0.4	−1.0189	−1.19499	−1.40842	−1.0190	−1.19493	−1.40847
0.1	0.6	−1.0216	−1.22544	−1.42402	−1.0219	−1.22541	−1.42400

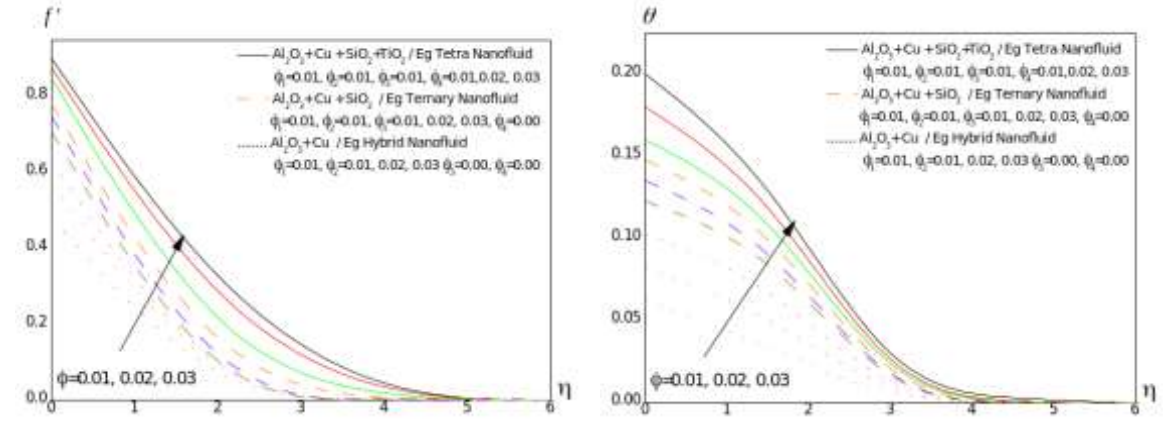
5. Results and discussion

The numerical solution is now interrogated parameter by parameter. Throughout this section the dimensionless velocity f′(η) and temperature θ(η) are compared for three ethylene-glycol (EG) based suspensions of increasing compositional complexity: the binary hybrid Al_2O_3–Cu/EG, the ternary hybrid Al_2O_3–Cu–SiO_2/EG and the tetra-hybrid Al_2O_3–Cu–SiO_2–TiO_2/EG. Unless a different value is quoted on the figure itself, every computation uses the baseline set $G = 2$, $K = 0.2$, $M = 0.3$, $f_s = 0.1$, $R_d = 0.5$, $Ec = 0.1$, $Q = 0.5$, $B_1 = 0.1$, $B_2 = 0.2$, $D_s = 0.1$, $Q_1 = 0.5$, $E_1 = 0.1$, $\delta = 0.2$ and $n = 0.2$, and only one parameter is varied at a time so that each trend reported below can be attributed unambiguously to a single physical mechanism.

The intervals have not been chosen arbitrarily. They are restricted to the window over which the constitutive closures used in Section 2 remain defensible: the Brinkman viscosity correlation and the Hamilton–Crosser conductivity rule are reliable only in the dilute regime, so the total solid loading is kept below about six per cent; the Rosseland diffusion approximation for the radiative flux requires an optically thick layer, which limits R_d to values of order unity; and the modified-Arrhenius source is written for moderate activation energies and temperature ratios, which bounds E_1 and δ. In every case the far-field conditions $f' \to 0$ and $\theta \to 0$ are satisfied asymptotically well inside the computational edge $\eta_\infty = 6$, which confirms that the finite domain does not contaminate the reported profiles.

Nanoparticle volume fraction, ϕ = 0.01–0.03 (Fig. 2). The loading of the last constituent of each suspension is stepped through 0.01, 0.02 and 0.03 while the remaining constituents are held at 0.01, so that the total solid fraction rises from 0.04 to 0.06 in the tetra-hybrid, from 0.03 to 0.05 in the ternary hybrid and from 0.02 to 0.04 in the binary hybrid. Both fields are lifted. The mechanism is the disparity in thermal conductivity between the dispersed phases and the carrier: copper (≈ 400 W m^{-1} K^{-1}), alumina

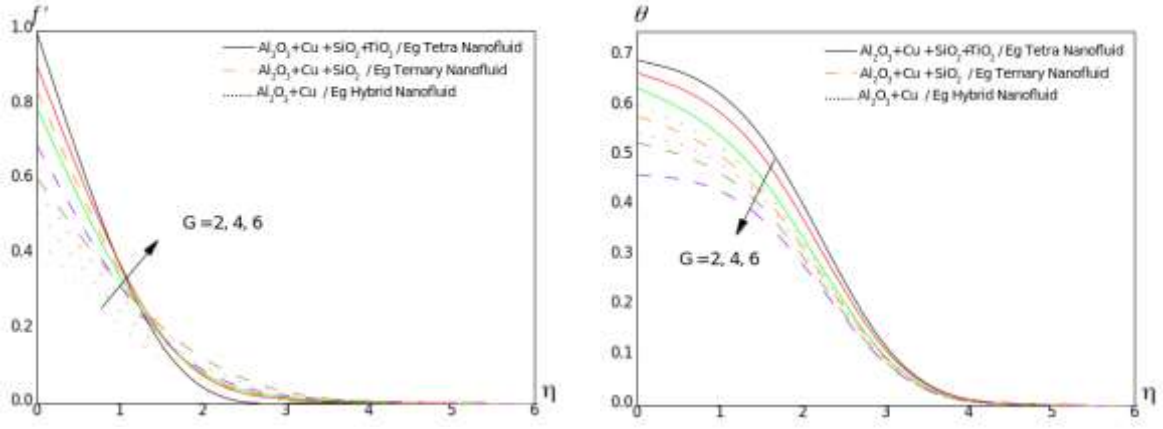
(≈ 40 W m^{-1} K^{-1}) and titania (≈ 8.9 W m^{-1} K^{-1}) exceed ethylene glycol (≈ 0.25 W m^{-1} K^{-1}) by one to three orders of magnitude, so each additional inclusion opens a further percolation path for heat and raises the effective conductivity of the mixture faster than the Brinkman relation raises its viscosity — over the range examined the conductivity gain is of the order of tens of per cent whereas the viscous penalty is only about 16%. Heat is therefore drawn further from the wall, the thermal layer widens, and the augmented thermal buoyancy overwhelms the additional viscous drag so that the stream accelerates. The ordering tetra > ternary > binary reflects the monotonic accumulation of high-conductivity surface area and is preserved at every η.



(a) (b)

Fig. 2. Influence of the solid volume fraction ϕ on (a) f′(η) and (b) θ(η), computed with G = 2, K = 0.2, M = 0.3, f_s = 0.1, R_d = 0.5, Ec = 0.1, Q = 0.5, B_1 = 0.1, B_2 = 0.2, D_s = 0.1, Pr = 6.2, Q_1 = 0.5, E_1 = 0.1, δ = 0.2 and n = 0.2.

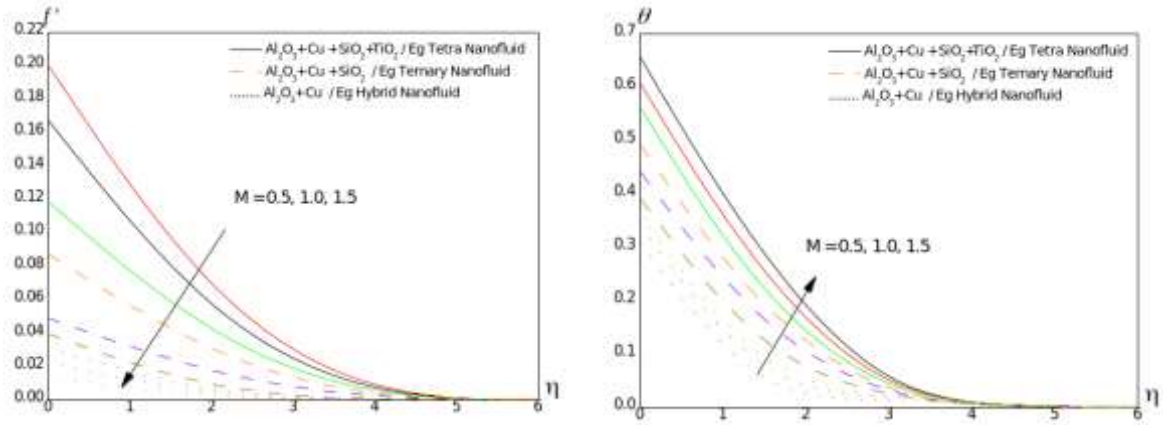
Grashof number, G = 2–6 (Fig. 3). G measures thermal buoyancy against viscous force, and tripling it from 2 to 6 moves the layer from the mixed-convection regime towards buoyancy dominance. The velocity responds with a pronounced acceleration and a near-wall maximum that both grows and migrates towards the surface, since the streamwise pressure defect created by the density deficit is directly proportional to G. The temperature behaves in the opposite sense: the intensified advection sweeps hot fluid downstream faster than conduction can replenish it, so the Péclet number based on layer thickness rises and the thermal layer is compressed rather than expanded. The tetra-hybrid again shows the strongest response because its larger effective volumetric expansion-to-density ratio $(\rho\beta)_{thnf}/\rho_{thnf}$ converts a given temperature excess into a larger body force.



(a) (b)

Fig. 3. **Influence of the Grashof number G on (a) f′(η) and (b) θ(η).**

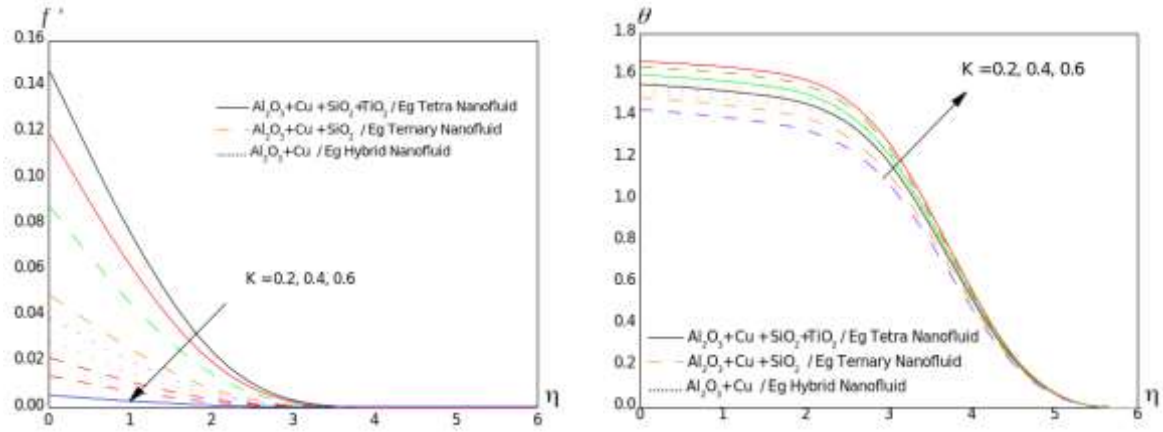
Magnetic parameter, M = 0.5–1.5 (Fig. 4). M is the squared ratio of the Lorentz force to the inertial force, so raising it from 0.5 to 1.5 triples the retarding body force $-\sigma B_0^2 u$ exerted on the electrically conducting suspension. The velocity falls throughout the layer and the momentum thickness contracts, the reduction being steepest close to the wall where the shear is largest. Two effects then raise the thermal field. First, the mechanical energy destroyed by the field is not lost but reappears as Ohmic dissipation, which enters the energy equation as a distributed source proportional to $M \cdot Ec \cdot (f')^2$. Second, the weakened advection lengthens the residence time of a fluid element next to the heated surface. The temperature is therefore elevated in the near-wall region, which is the classical trade-off of magnetic flow control: drag reduction of the boundary layer is bought at the cost of degraded convective heat transport.



(a) (b)

Fig. 4. **Influence of the magnetic parameter M on (a) f′(η) and (b) θ(η).**

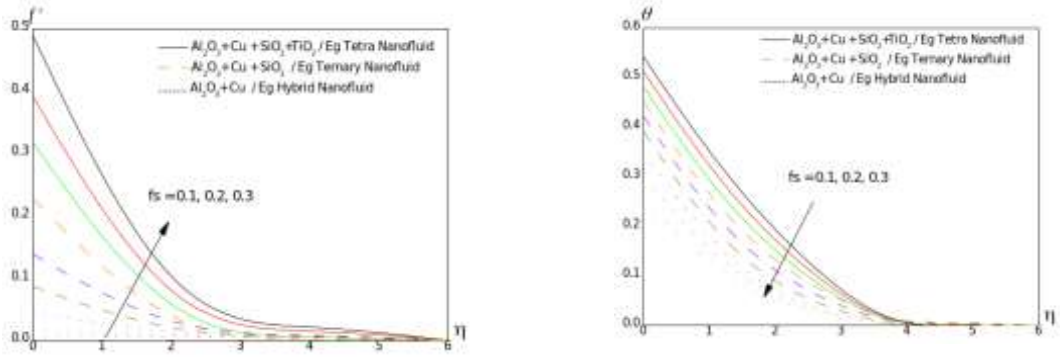
Inverse-Darcy parameter, K = 0.2–0.6 (Fig. 5). Because K is inversely proportional to the permeability, tripling it is equivalent to reducing the pore space available to the flow by a factor of three and hence stiffening the linear Darcian resistance $-(\mu/k_p)u$ by the same factor. The stream decelerates markedly. Fluid then lingers longer within the matrix, so conduction has more time to act on a given element before it is convected away; the temperature field is correspondingly elevated and the thermal layer thickens. The result illustrates why a porous insert is an effective thermal-storage device but a poor convective heat exchanger: it raises the local temperature level while suppressing the transport rate.



(a) (b)

Fig. 5. **Influence of the inverse-Darcy parameter K on (a) f′(η) and (b) θ(η).**

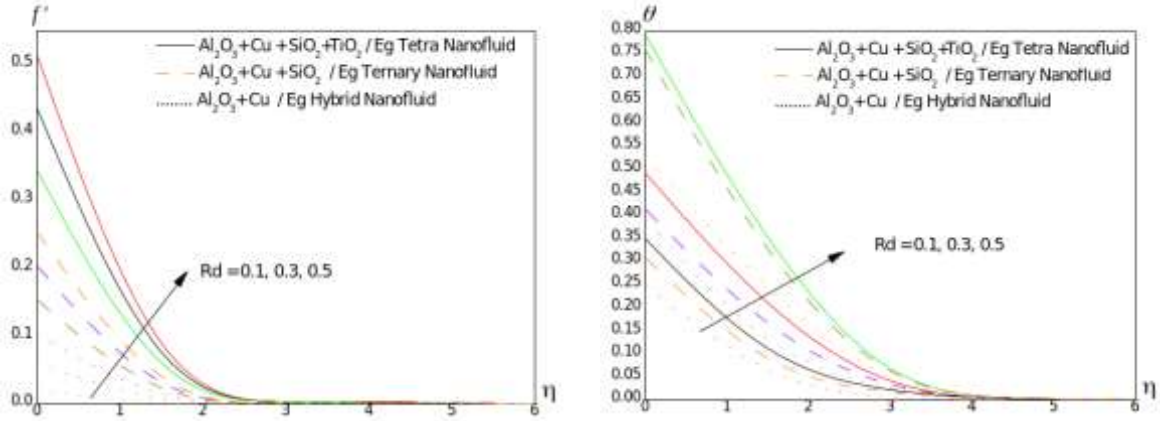
Forchheimer parameter, f_s = 0.1–0.3 (Fig. 6). The Forchheimer term supplies the quadratic, form-drag correction to Darcy's law that becomes significant once the pore Reynolds number exceeds unity, and it enters the momentum equation as $-f_s(f')^2$. Its influence is therefore concentrated where the velocity is largest, near the wall, and it grows nonlinearly rather than linearly with the parameter. Increasing f_s from 0.1 to 0.3 retards the stream and, by the same residence-time argument advanced for K, broadens the thermal layer so that θ is raised. The response is qualitatively identical to that of K but is distributed differently across the layer, being negligible in the outer region where f′ is small and appreciable in the core of the momentum layer.



(a) (b)

Fig. 6. **Influence of the Forchheimer parameter f_s on (a) f′(η) and (b) θ(η).**

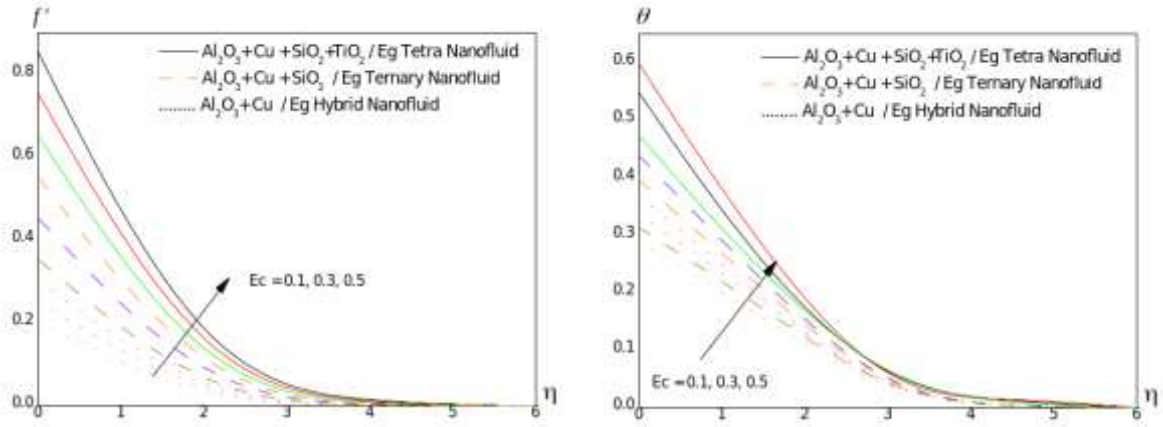
Radiation parameter, R_d = 0.1–0.5 (Fig. 7). Under the Rosseland approximation radiative transfer is absorbed into the energy equation as an additive diffusivity, the effective conduction coefficient carrying the factor $(4/3)R_d(1 + \delta\theta)^3$. Raising R_d from 0.1 to 0.5 therefore lifts that coefficient by roughly 47% at the baseline temperature ratio and supplies a transport route that operates in parallel with conduction and convection rather than in competition with them. Energy is deposited throughout the layer instead of being confined to the conduction sublayer, so the temperature rises at every η and the thermal thickness grows. The additional buoyancy generated by the hotter fluid produces the modest gain seen in the velocity profile. Radiative augmentation is thus the most efficient of the mechanisms examined here for raising the temperature level without paying a momentum penalty, and it is also the mechanism most sensitive to the retention of the full fourth-power dependence: a linearised treatment would understate the effect appreciably at the larger values of δ.



(a) (b)

Fig. 7. **Influence of the radiation parameter R_d on (a) f′(η) and (b) θ(η).**

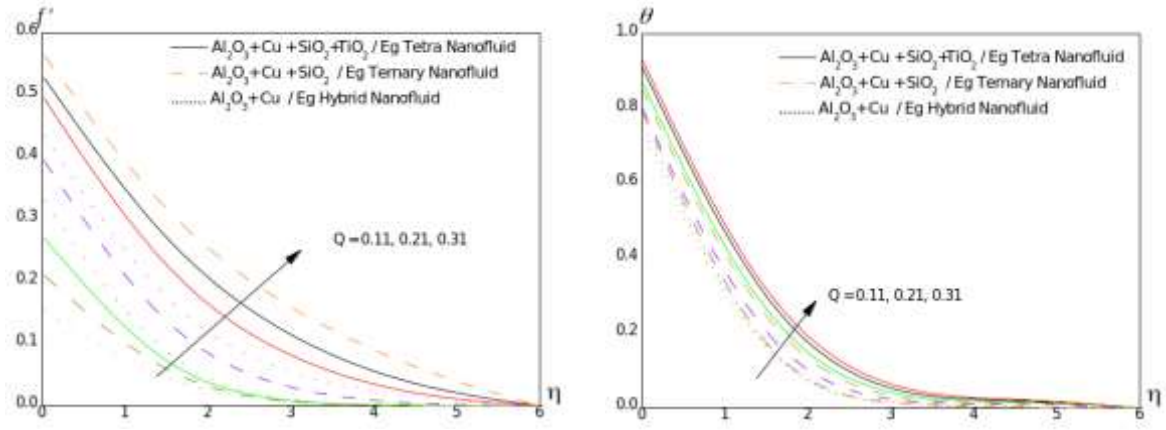
Eckert number, Ec = 0.1–0.5 (Fig. 8). Ec is the ratio of the kinetic energy of the stream to the enthalpy difference driving the heat transfer, and a fivefold increase multiplies the irreversible frictional-heating term $Ec(f'')^2$ by the same factor. Mechanical energy extracted from the mean flow is converted into internal energy, most intensely where the shear rate is greatest, so the temperature rise is sharpest in the immediate neighbourhood of the wall and can flatten the near-wall gradient appreciably. Buoyancy then communicates the effect to the velocity field. Because dissipation heats the fluid adjacent to the surface, it narrows the wall-to-fluid temperature difference and is the principal reason for the deterioration of the Nusselt number reported in Section 5.1.



(a) (b)

***Fig. 8.* Influence of the Eckert number Ec on (a) f′(η) and (b) θ(η).**

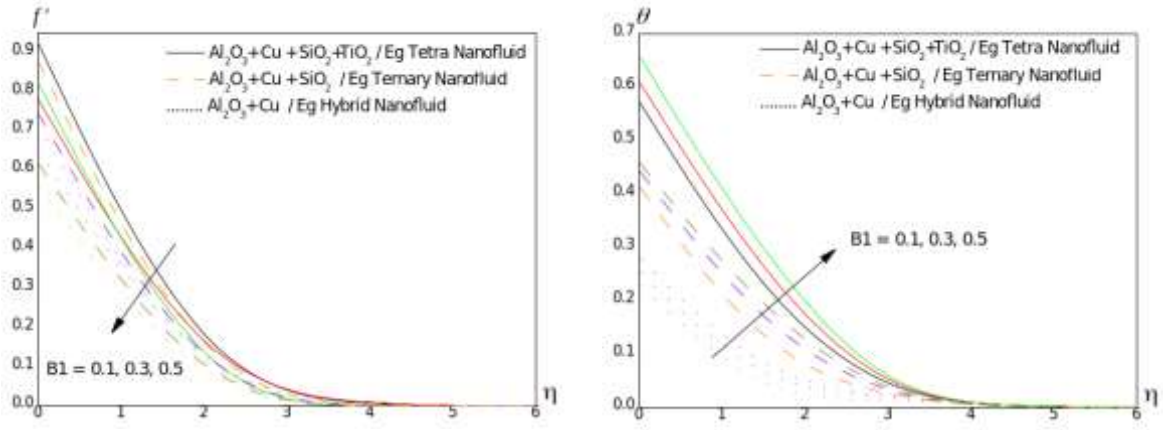
Heat-source parameter, Q = 0.11–0.31 (Fig. 9). Q represents volumetric internal generation and acts as a distributed source that is independent of the local gradients, so raising it by a factor of roughly three adds thermal energy uniformly throughout the layer. The temperature climbs appreciably while the velocity gains only slightly, since the extra buoyancy is partly offset by the reduced density of the heated fluid. The practical significance is that internal generation degrades the wall heat flux by raising the fluid temperature towards that of the surface, an effect that must be accounted for in any reactor or electronics-cooling application in which the working fluid is itself a heat source.



(a) (b)

Fig. 9. Influence of the heat-source parameter Q on (a) f′(η) and (b) θ(η).

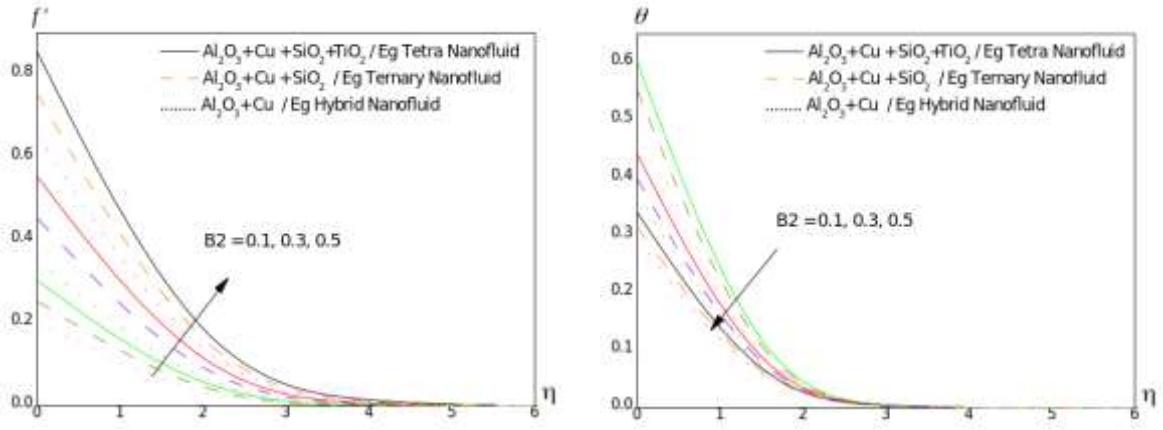
Velocity-slip parameter, B_1 = 0.1–0.5 (Fig. 10). Navier slip replaces the no-slip constraint by $f'(0) = 1 + B_1 f''(0)$, so increasing B_1 fivefold relaxes the shear constraint at the surface and allows the liquid immediately adjacent to it to move faster. The velocity therefore increases near the wall while the wall shear gradient, and with it the skin friction, is reduced. Because the slipping fluid is less strongly coupled to the surface, less momentum — and hence less thermal signal — is transmitted from the wall into the layer, so θ falls slightly. Slip of this magnitude is characteristic of rarefied conditions, microchannel geometries and hydrophobic or textured surfaces, and the result quantifies the modest thermal penalty that accompanies the drag benefit.



(a) (b)

Fig. 10. **Influence of the velocity-slip parameter B_1 on (a) f′(η) and (b) θ(η).**

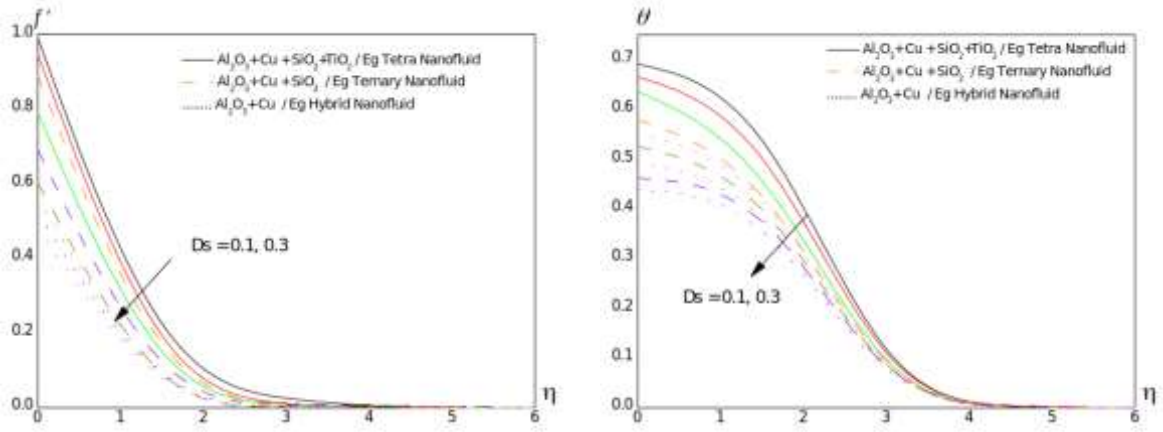
Thermal-slip parameter, B_2 = 0.1–0.5 (Fig. 11). A temperature jump at the wall, $\theta(0) = 1 + B_2\theta'(0)$, interposes a finite interfacial resistance between the heated surface and the fluid. As B_2 is raised from 0.1 to 0.5 a progressively smaller fraction of the imposed thermal potential is actually delivered to the liquid, so the temperature falls at every η and the thermal layer thins. Because the thermal field is the source of the buoyancy that drives the motion, the velocity is depressed as well. Thermal slip is thus the most effective single means of suppressing both fields simultaneously, and it is the parameter to which the Nusselt number is most sensitive — which makes the quality of the wall contact, rather than the choice of coolant, the first thing to check when a compact exchanger underperforms.



(a) (b)

Fig. 11. **Influence of the thermal-slip parameter B_2 on (a) f′(η) and (b) θ(η).**

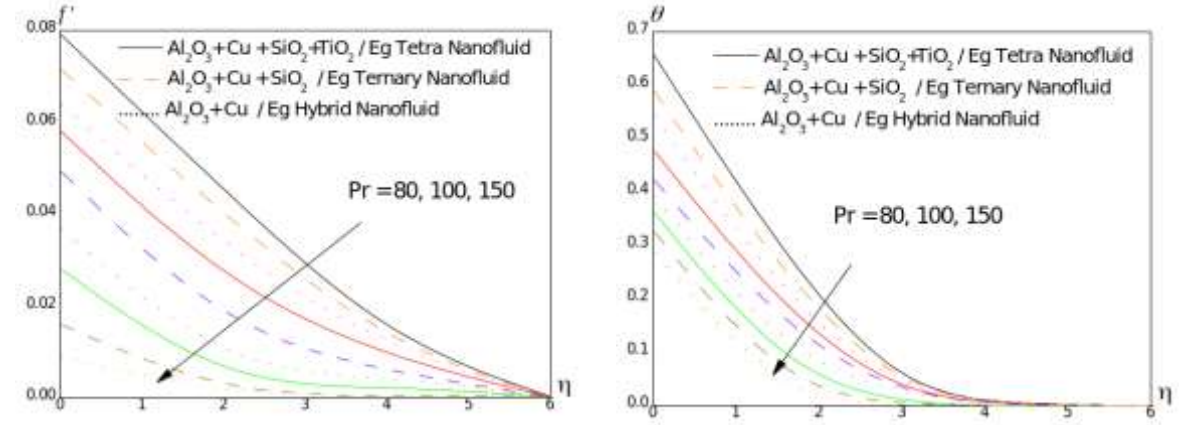
Thermal-dispersion parameter, D_s = 0.1–0.3 (Fig. 12). Mechanical dispersion in a porous medium arises from the tortuous, velocity-dependent mixing of fluid at the pore scale and is modelled here as an additional conductivity proportional to the local velocity, $D_s f'$. Raising D_s therefore augments the effective thermal diffusivity precisely where the flow is fastest, and the consequence is a redistribution rather than an accumulation of energy: heat is carried away from the immediate neighbourhood of the wall more efficiently, the interior of the layer is stirred more vigorously, and the wall gradient $-\theta'(0)$ steepens. Because the wall carries a temperature jump, the sharper gradient also depresses $\theta(0)$ itself. The enhancement is largest for the tetra-hybrid, whose stagnant effective conductivity is already the highest of the three, so that the dispersive and molecular contributions reinforce rather than merely add to one another — this is the clearest evidence in the present results that pore-scale stirring and compositional complexity are complementary design levers rather than alternatives.



(a) (b)

Fig. 12. Influence of the thermal-dispersion parameter D_s on (a) $f'(\eta)$ and (b) $\theta(\eta)$.

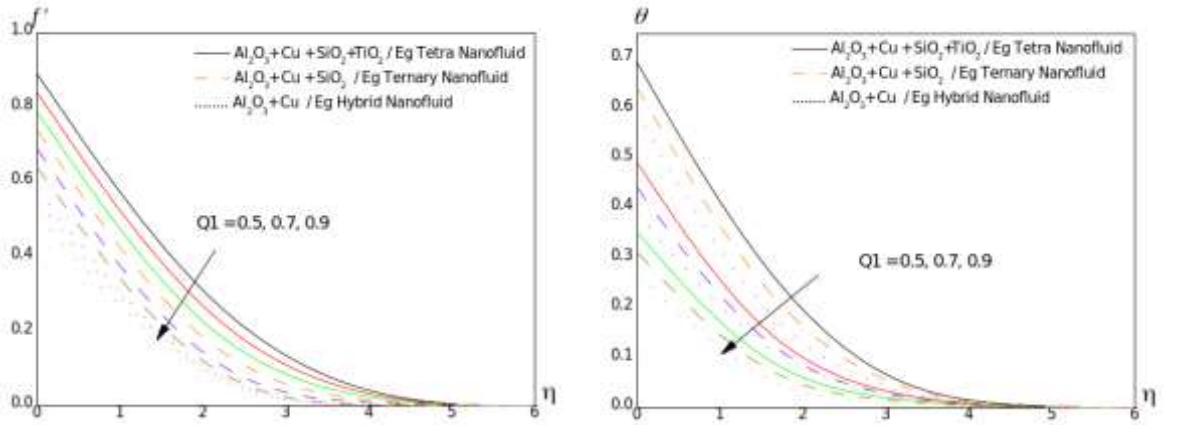
Prandtl number, Pr = 80–150 (Fig. 13). The values scanned correspond to ethylene glycol over a realistic operating window, the smaller figure representing the warmer and less viscous state. Since $Pr = \nu/\alpha$, a larger value implies a smaller thermal diffusivity relative to momentum diffusivity: heat is transported away from the wall less readily than momentum, the thermal layer contracts and the temperature falls. In free-convection scaling the thermal thickness varies roughly as $Pr^{-1/2}$, so the change from Pr = 80 to Pr = 150 is expected to thin the layer by about a quarter, which is consistent with the computed profiles. The attendant loss of buoyancy lowers the velocity; the tetra-hybrid nevertheless retains the best thermal performance of the three suspensions at every Pr, because its higher effective conductivity partially offsets the reduction in diffusivity.



(a) (b)

Fig. 13. **Influence of the Prandtl number Pr on (a) f′(η) and (b) θ(η).**

Exothermicity parameter, Q_1 = 0.5–0.9 (Fig. 14). Q_1 is the Frank–Kamenetskii number and measures the heat liberated by the exothermic step against the conductive capacity of the layer. Since the reactant is present in excess and its depletion is neglected, the reaction acts as a purely additive volumetric source, and raising Q_1 therefore deposits energy throughout the layer at a rate that itself increases with the local temperature. The temperature climbs accordingly and the thermal layer thickens, while the associated buoyancy lifts the velocity. The positive feedback embodied in the source term — hotter fluid reacts faster, which makes it hotter still — is the reason the response is more than proportional to Q_1, and it is also the reason the parameter must be bounded: beyond the range examined here the conductive removal of heat can no longer balance its generation and the steady solution is lost to thermal runaway, a limit of direct concern in the design of reactive coolant circuits.

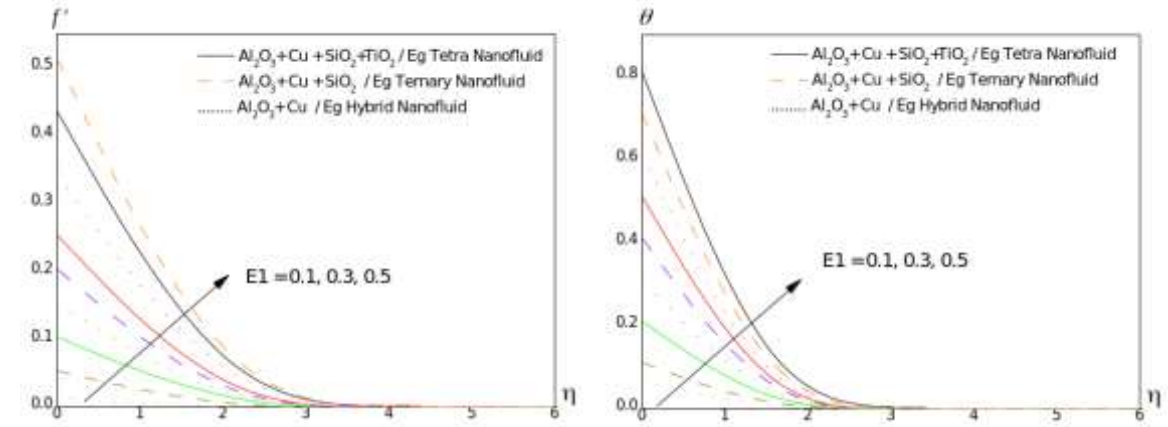


(a) (b)

Fig. 14. **Influence of the exothermicity parameter Q_1 on (a) f′(η) and (b) θ(η).**

Activation-energy parameter, E_1 = 0.1–0.5 (Fig. 15). In the modified Arrhenius law the rate constant carries the factor $\exp[-E_1/(1+\delta\theta)]$, so activation energy acts as an energetic barrier that fewer molecular collisions can surmount. Raising E_1 from 0.1 to 0.5 reduces that exponential factor by roughly a third at the baseline temperature ratio, so less heat is liberated per unit volume and the temperature falls throughout the layer. The weakened buoyancy depresses the velocity in turn. The trend is the exact mirror image of

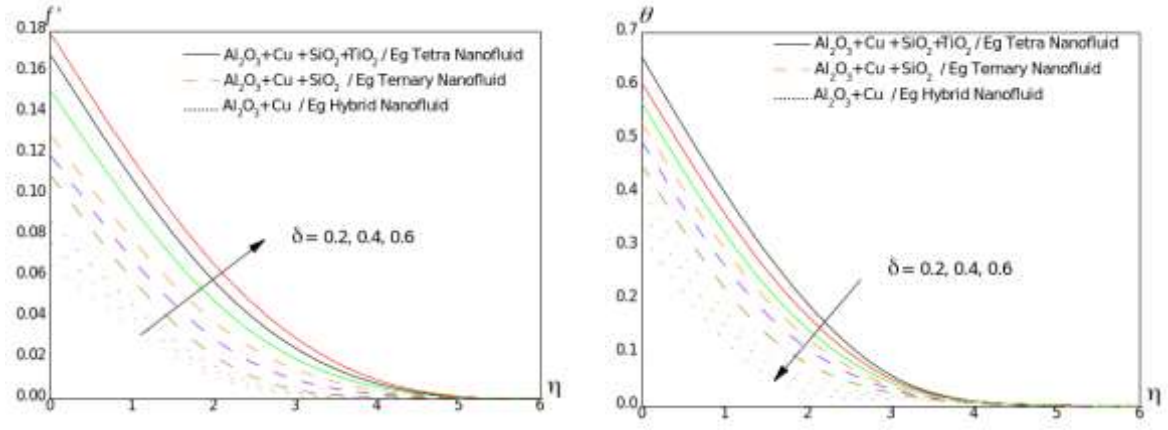
that produced by Q_1, as it must be, since the two parameters enter the same source term with opposite sense; and because the wall-to-fluid temperature difference is thereby restored, E_1 is one of the few parameters examined that improves the Nusselt number.



(a) (b)

Fig. 15. **Influence of the activation-energy parameter E_1 on (a) f′(η) and (b) θ(η).**

Temperature-ratio parameter, δ = 0.2–0.6 (Fig. 16). δ is the ratio of the wall-to-ambient temperature excess to the ambient temperature and therefore sets the strength of the temperature dependence of both the radiative flux and the Arrhenius rate constant. Tripling it acts on the thermal field twice over: the radiative conductivity carries the factor $(1 + \delta\theta)^3$ and rises steeply, while the exponent $-E_1/(1 + \delta\theta)$ is simultaneously weakened so that the exothermic source becomes more vigorous. Both mechanisms push in the same direction, the thermal layer thickens and the temperature rises, and the velocity follows through buoyancy. Large δ corresponds to a strongly non-isothermal system in which the linearisation commonly applied to the radiative term would fail, which is why the full temperature-ratio formulation has been retained here.

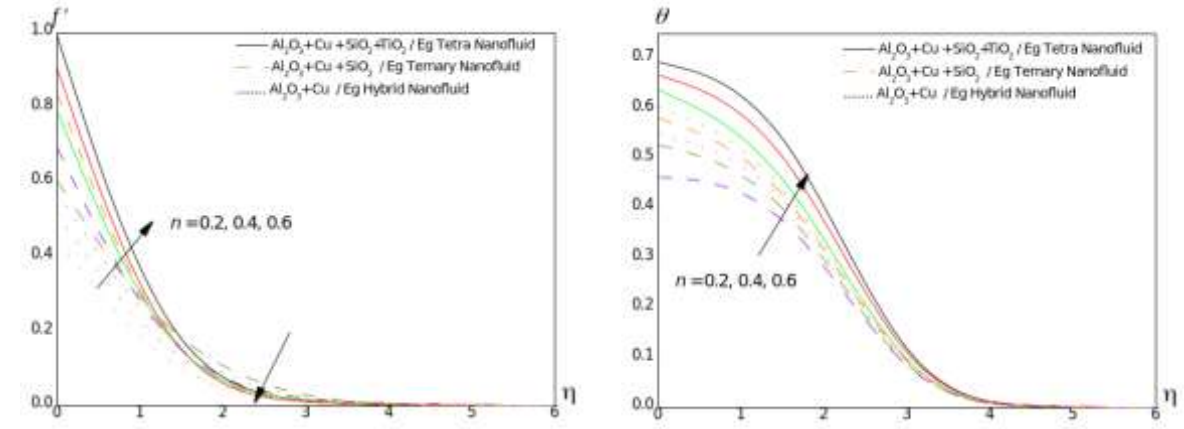


(a) (b)

Fig. 16. **Influence of the temperature-ratio parameter δ on (a) f′(η) and (b) θ(η).**

Arrhenius temperature exponent, n = 0.2–0.6 (Fig. 17). The exponent n is the fitted power of the temperature ratio carried by the modified-Arrhenius rate constant and therefore controls how sharply the

exothermic source responds to heating beyond the response already contained in the exponential. Larger values steepen that response, so more heat is released in the hotter part of the layer, the temperature rises and the thermal layer thickens, and the enhanced buoyancy strengthens the velocity field. The monotonic behaviour over $0.2 \leq n \leq 0.6$ indicates that the solution remains well posed throughout the range, with no sign of the multiple branches that can appear when the source term is made more strongly temperature-sensitive still.



(a) (b)

Fig. 17. **Influence of the Arrhenius temperature exponent n on (a) f′(η) and (b) θ(η).**

5.1. Wall transfer characteristics

Figures 18–24 collect the engineering quantities of Eqs. (11) and (12) as functions of the controlling parameters, computed for all three suspensions. In every suspension the magnitude of the wall shear increases with G, M, K, f_s, Q, R_d, Ec and D_s, and is relieved by B_1 and B_2. The Nusselt number is depressed by R_d, Ec, Q, B_2, Pr, δ and Q_1, and raised by D_s, φ_i and E_1. The pattern is coherent: any mechanism that deposits heat within the layer — radiation, dissipation, internal generation, the exothermic step — narrows the wall-to-fluid temperature difference and therefore degrades the wall heat flux, whereas mechanisms that improve the transport of heat away from the wall, principally dispersion and increased solid loading, sharpen the gradient and improve it. For every parameter examined the four-particle fluid returns the largest rate of heat transfer, which confirms that its transport capacity exceeds that of the ternary and binary hybrids.

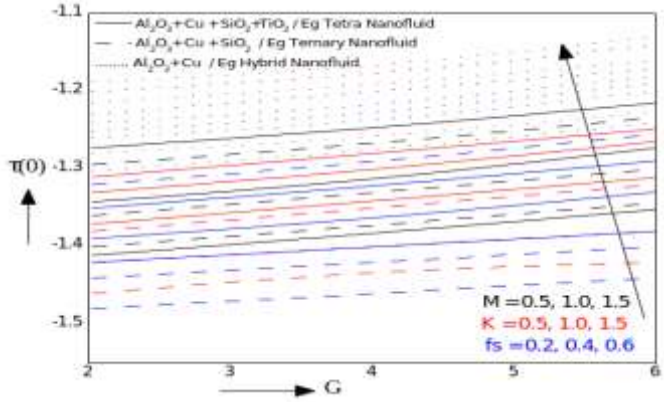


Fig. 18. **Skin friction as a function of G for several values of M, K and f_s.**

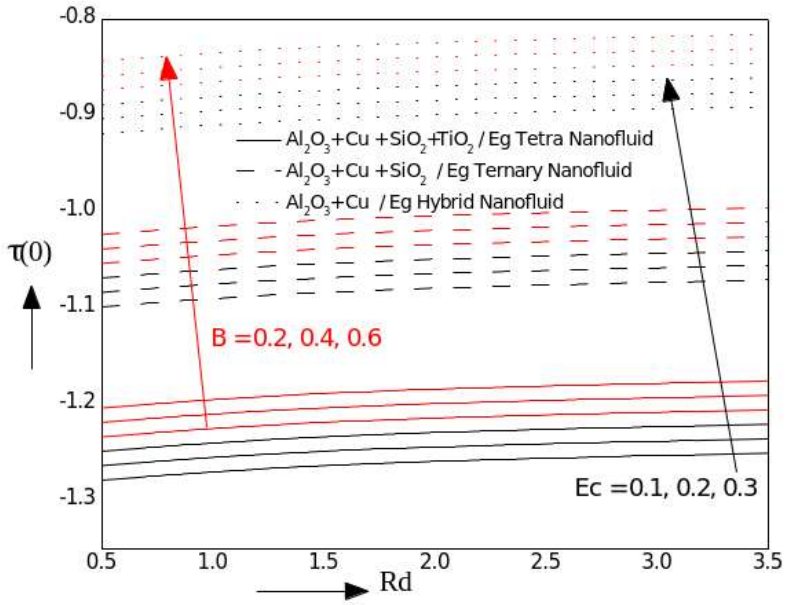


Fig. 19. **Skin friction as a function of R_d for several values of Ec and B_1.**

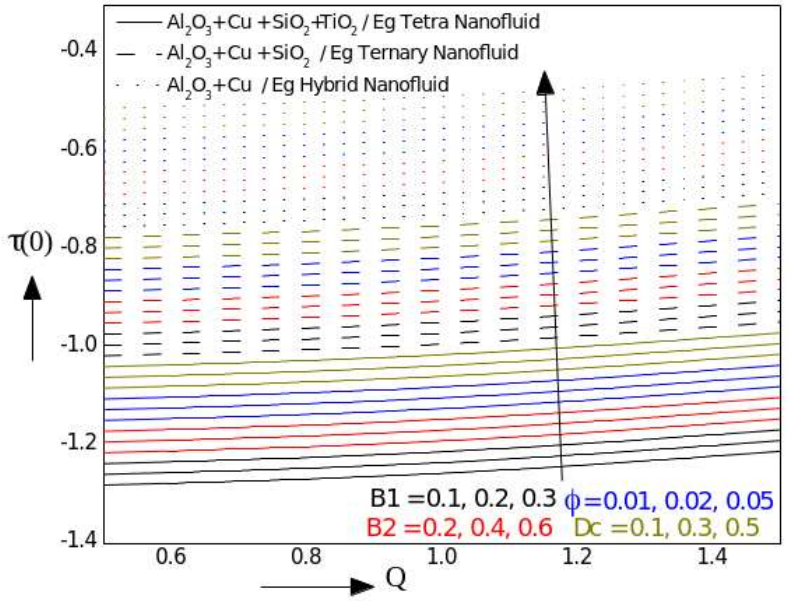


Fig. 20. **Skin friction as a function of Q for several values of B_1, B_2 and φ_i.**

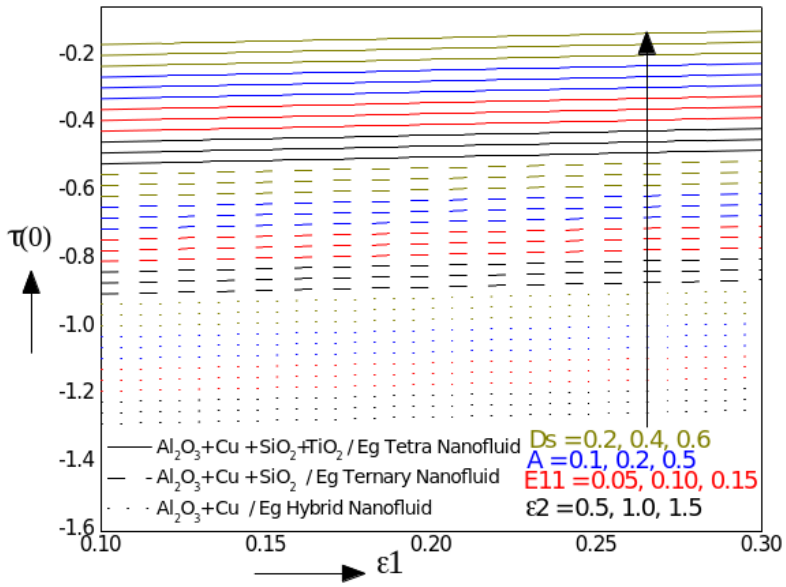


Fig. 21. **Skin friction as a function of ε_1 for several values of ε_2, D_s, A and E_1.**

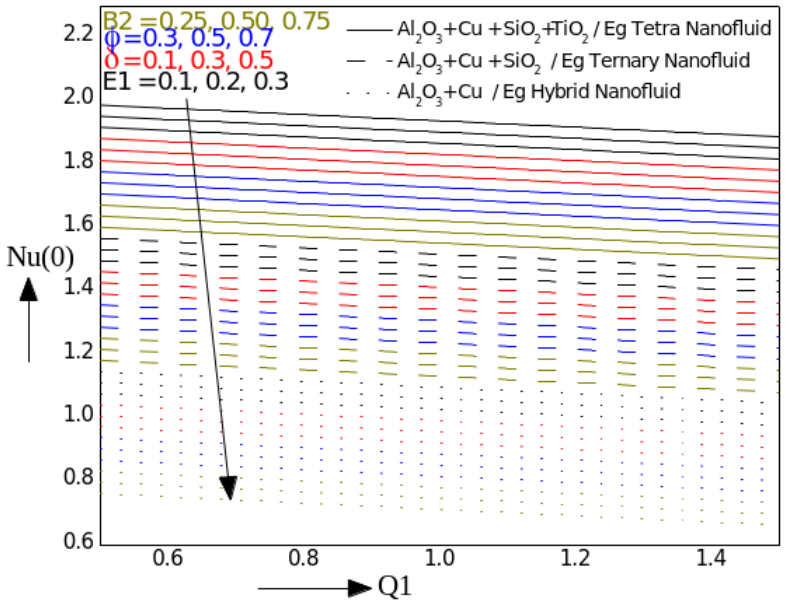


Fig. 22. **Nusselt number as a function of Q_1 for several values of E_1, δ, φ_i and B_2.**

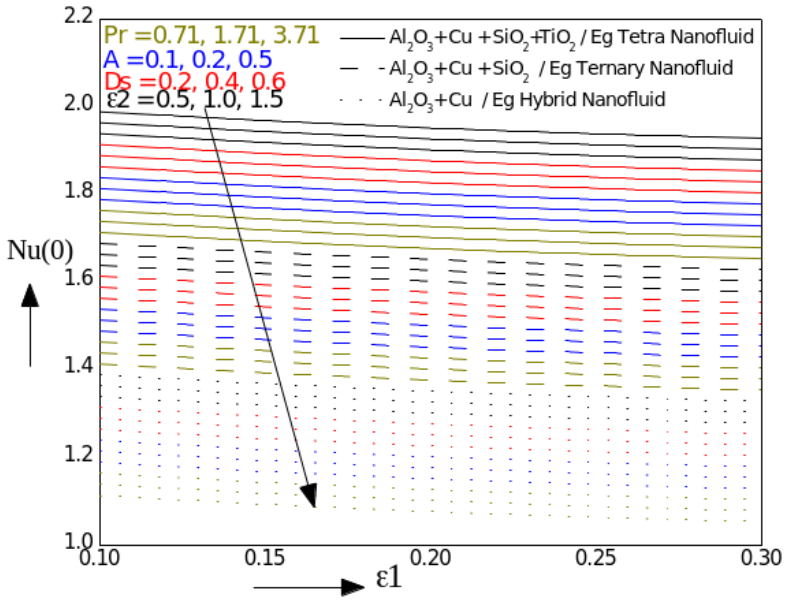


Fig. 23. **Nusselt number as a function of ε_1 for several values of ε_2, D_s, A and Pr.**

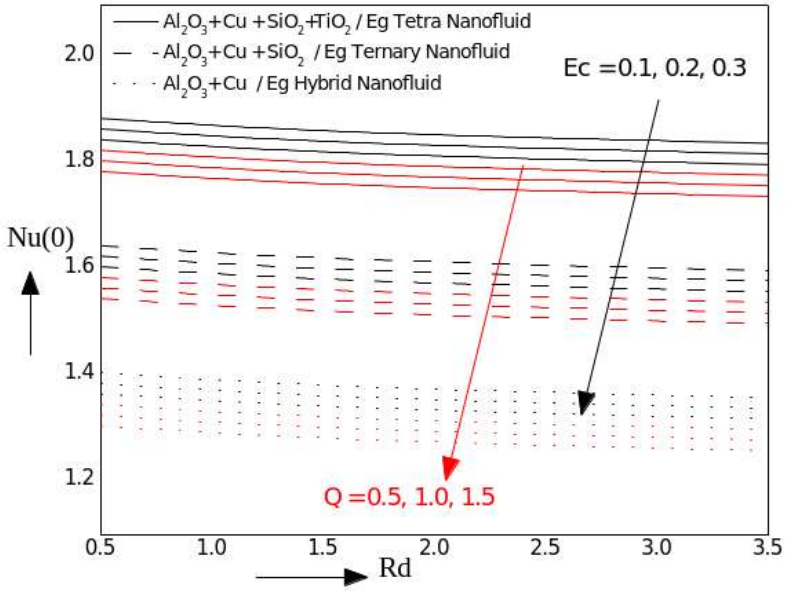


Fig. 24. **Nusselt number as a function of R_d for several values of Ec and Q.**

6. Concluding remarks

The foregoing analysis has treated non-Darcy magnetohydrodynamic convective heat transport in an ethylene-glycol-based four-component nanoparticle suspension driven by a linearly stretched sheet, retaining simultaneously velocity-proportional thermal dispersion, nonlinear radiative exchange, a modified-Arrhenius exothermic source, thermally sensitive viscosity, conductivity and electrical conductivity, Joule and viscous heating, and independent velocity and thermal slips. The principal outcomes are as follows.

- Increasing the Grashof number accelerates the stream and compresses the thermal layer, so that the wall heat transfer improves and the magnitude of the skin friction grows with it.

- Magnetic and porous resistances alike retard the motion while raising the temperature, so that the Nusselt number is reduced; drag control and heat-transfer performance are therefore in direct opposition in this configuration.
- Radiative transfer, frictional heating and internal generation all widen the thermal layer and lift the temperature, and in consequence the Nusselt number drops. Retaining the full fourth-power radiative dependence matters at the larger temperature ratios, where a linearised treatment would understate the effect.
- Velocity slip strengthens the near-wall motion and relieves the wall shear at a small thermal cost. Thermal slip acts far more severely, weakening the interfacial exchange of heat so that both fields are depressed and the Nusselt number falls with them; it is the single parameter to which the wall heat flux is most sensitive.
- A greater volume fraction of solids raises both profiles and improves the wall heat-transfer rate, the ordering tetra > ternary > binary being preserved at every η.
- Thermal dispersion redistributes energy within the layer, steepens the wall gradient and improves the heat-transfer characteristic, and its benefit is largest for the suspension whose stagnant conductivity is already highest — dispersive and molecular conduction reinforce one another rather than merely adding.
- A more vigorous exothermic step, whether through a larger Frank–Kamenetskii number, a larger temperature ratio or a larger Arrhenius exponent, lifts the temperature and the velocity while degrading the wall heat flux, whereas a higher activation energy suppresses the source and restores it.

Across the entire parameter space investigated, the four-component suspension (Al_2O_3 + Cu + SiO_2 + TiO_2/EG) sustains its superiority over the ternary and binary fluids in both transported quantities — velocity and temperature alike — while simultaneously yielding the highest wall heat-transfer rate. This consistent advantage is attributable to the synergistic cooperation among its four constituent nanoparticles and its enhanced effective thermal conductivity. Notably, the wall shear stress of the quaternary nanofluid exceeds that of the two-particle hybrid by roughly 37–39%. These characteristics position the fluid as a compelling choice for solar-thermal absorbers, ambient-energy harvesting devices and other next-generation thermal-engineering applications. Natural extensions of the present work include unsteady and three-dimensional formulations, a comprehensive entropy-generation analysis, relaxation of the excess-reactant assumption so that the approach to thermal runaway can be tracked, and experimental validation of the predicted performance gains.

References

1. Chamkha, A. J., Miroshnichenko, I. V., & Sheremet, M. A. (2017). Numerical analysis of unsteady conjugate natural convection of hybrid water-based nanofluid in a semicircular cavity. *Journal of Thermal Science and Engineering Applications, 9*(4), 041004. https://doi.org/10.1115/1.4036203
2. Jan, A., Nawaz, R., & Ahmad, A. (2024). Non-similar analysis of radially magnetized flow and heat transfer of Reiner–Philippoff based nanofluid over a curved stretching surface with viscous dissipation. *International Journal of Thermofluids, 22*, 100657. https://doi.org/10.1016/j.ijft.2024.100657
3. Sachhin, S. M., Nagegowda, K., Mahabaleshwar, U. S., Pérez, L. M., & Lorenzini, G. (2026). Joule heating and viscosity-ratio effects on dissipative ternary nanofluid flow over a permeable surface.

International Journal of Computational Methods and Experimental Measurements, 14(1), 57–80. https://doi.org/10.56578/ijcmem140104

4. Rajhi, W., Ben Hamida, M. B., Adnan, Walelign, T., Ahmad, H., Khan, S. U., & Alrasheedi, N. (2025). Comparative study of thermal response for tetra nanofluid through a vertically oriented needle device inspired by combined convection and porous media. *Scientific Reports, 15*, 36506. https://doi.org/10.1038/s41598-025-20648-9
5. Mkhatshwa, M. P. (2025). Numerical study of Ellis-micropolar tetra-hybrid nanofluid flow over a stretching surface with g-jitter and magnetic dipole. *Multiscale and Multidisciplinary Modeling, Experiments and Design, 8*, 450. https://doi.org/10.1007/s41939-025-01051-3
6. Choudhary, P., Loganathan, K., Jat, K., Arunachalam, K. P., & Eswaramoorthi, S. (2025). Thermal and velocity slip impacts on MHD tetra-hybrid nanofluids flow over a porous stretching surface. *Discover Applied Sciences, 7*, 720. https://doi.org/10.1007/s42452-025-07359-6
7. Kvernvold, O., & Tyvand, P. A. (1980). Dispersion effects on thermal convection in porous media. *Journal of Fluid Mechanics, 99*(4), 673–686. https://doi.org/10.1017/S0022112080000821
8. Cheng, P. (1981). Thermal dispersion effects in non-Darcian convective flows in a saturated porous medium. *Letters in Heat and Mass Transfer, 8*, 313–321.
9. Telles, R. S., & Trevisan, O. V. (1993). Dispersion in heat and mass transfer natural convection along vertical boundaries in porous media. *International Journal of Heat and Mass Transfer, 36*(5), 1357–1365. https://doi.org/10.1016/S0017-9310(05)80103-6
10. Razzaq, I., Ali, A. B. M., Wang, X., Rasool, G., Formanova, S., & Kallel, M. (2026). Further insights into the effects of magnetism and thermal radiation on Al_2O_3–Cu/engine oil hybrid nanofluid flow in Darcy–Forchheimer porous media. *Modern Physics Letters B, 40*(3), 2550279. https://doi.org/10.1142/S0217984925502793
11. Takreem, K. M., & Satya Narayana, P. V. (2023). Impacts of Joule heating and dissipation on magnetohydrodynamic ternary-hybrid nanofluid (Al_2O_3–TiO_2–SiO_2/H_2O) flow over an elongated sheet with Darcy–Forchheimer medium. *Proceedings of the Institution of Mechanical Engineers, Part E: Journal of Process Mechanical Engineering, 239*(2), 821–829. https://doi.org/10.1177/09544089231200381
12. Moltot, A. T., Gorfie, E. H., Zergaw, G. A., & Dessie, H. (2025). Unsteady MHD flow of tangent hyperbolic ternary hybrid nanofluid in a Darcy–Forchheimer porous medium over a permeable stretching sheet with variable thermal conductivity. *F1000Research, 14*, 152. https://doi.org/10.12688/f1000research.158629.2
13. Khalil, S., Abbas, T., & Nawaz, R. (2025). Enhanced thermal and flow behavior of Cu–Al_2O_3/water hybrid nanofluids in porous media under variable magnetic field conditions. *International Journal of Thermofluids, 27*, 101166. https://doi.org/10.1016/j.ijft.2025.101166
14. Moltot, A. T., Gorfie, E. H., Zergaw, G. A., & Asress, H. D. (2025). Influences of variable thermal conductivity, viscous dissipation, and Cattaneo–Christov heat and mass fluxes on MHD tangent hyperbolic ternary hybrid nanofluid flow over a stretching sheet. *Engineering Reports, 7*, e70291. https://doi.org/10.1002/eng2.70291
15. Al-Atawi, N. O. (2026). Mathematical modeling for nonlinear slippery-hybrid nanofluid flow with radiation impacts and thermophoretic diffusion via a porous medium. *Discover Nano, 21*(1), 35. https://doi.org/10.1186/s11671-026-04456-2

16. Khan, M. N., Ahmad, S., Wang, Z., Hussien, M., Alhuthali, A. M. S., & Ghazwani, H. A. (2024). Flow and heat transfer insights into a chemically reactive micropolar Williamson ternary hybrid nanofluid with cross-diffusion theory. *Nanotechnology Reviews, 13*(1), 20240081. https://doi.org/10.1515/ntrev-2024-0081
17. Venkateswarlu, B., Chavan, S., Joo, S. W., & Kim, S. C. (2024). Entropy analysis of electromagnetic trihybrid nanofluid flow with temperature-dependent viscosity in a Darcy–Forchheimer porous medium over a stretching sheet under convective conditions. *Journal of Molecular Liquids, 393*, 123660. https://doi.org/10.1016/j.molliq.2023.123660
18. Joshi, M., & Reddy, G. V. R. (2025). Energy transport in a MHD hybrid nanofluid flow over a porous exponentially stretching sheet. *East European Journal of Physics*, (4), 298–307. https://doi.org/10.26565/2312-4334-2025-4-28
19. Faizan, M., Zafar, S. S., Ali, F., Khan, U., Zaib, A., & Khashi'ie, N. S. (2026). Radiative features of Darcy–Forchheimer flow of entropy-optimized Cross flow conveying ternary hybrid nanofluid past a stretching cylinder. *Frontiers in Heat and Mass Transfer*, *24*(1), 5. https://doi.org/10.32604/fhmt.2026.075018
20. Khan, M., & Rasheed, A. (2021). Slip velocity and temperature jump effects on molybdenum disulfide MoS_2 and silicon oxide SiO_2 hybrid nanofluid near irregular 3D surface. *Alexandria Engineering Journal, 60*(1), 1689–1701. https://doi.org/10.1016/j.aej.2020.11.019
21. Mingyu, Z., & Jing, W. (2024). Effects of interfacial velocity or temperature slips on finite line contact thermal EHL in simple sliding motion. *Tribology, 44*(8), 1092–1106. https://doi.org/10.16078/j.tribology.2023110
22. Maranna, T., Sachin, G. M., Mahabaleshwar, U. S., Pérez, L. M., & Shevchuk, I. V. (2024). Impact of Navier's slip and MHD on a hybrid nanofluid flow over a porous stretching/shrinking sheet with heat transfer. *Fluids, 9*(8), 180. https://doi.org/10.3390/fluids9080180
23. Cheng, P. (1981). Thermal dispersion effects in non-Darcian convective flows in a saturated porous medium. *Letters in Heat and Mass Transfer, 8*, 313–321.
24. Telles, R. S., & Trevisan, O. V. (1993). Dispersion in heat and mass transfer natural convection along vertical boundaries in porous media. *International Journal of Heat and Mass Transfer, 36*(5), 1357–1365. https://doi.org/10.1016/S0017-9310(05)80103-6
25. Seddeek, M. A., & Salem, A. M. (2005). Laminar mixed convection adjacent to vertical continuously stretching sheet with variable viscosity and variable thermal diffusivity. *International Journal of Heat and Mass Transfer, 41*, 1048–1055.
26. Zegeye, G. B., Haile, E., & Awgichew, G. (2024). Viscous dissipation and Joule heating effects of Carreau nanofluid axisymmetric flow past unsteady radially stretching porous disk. *International Journal of Thermofluids, 22*, 100655. https://doi.org/10.1016/j.ijft.2024.100655